

# Steady And Unsteady Bubbly Two-Phase Flow (Gas-Liquid Flow) Around A Hydrofoil In Enlarging Rectangular Channel

Laith Jaafer Habeeb<sup>1</sup>, Riyadh S. Al-Turaihi<sup>2</sup>

<sup>1</sup>Mechanical Engineering Dept., University of Technology, Baghdad(10) – Iraq

<sup>2</sup>College of Engineering/ Dept. of Mech. Eng., Babylon University, Babil(30) – Iraq

## ABSTRACT

Experimental and numerical studies are investigated to study the two-phase flow phenomena around straight hydrofoil for different angle of attacks in a rectangular enlarging channel which has the dimensions (10 × 3 × 70 cm) enlarged from assembly circular tube of the two phases. Experiments are carried out in the channel with air-water flow with different air and water flow rates. These experiments are aimed to visualize the two phase flow phenomena as well as to study the effect of pressure difference through the channel with the existence of the hydrofoil. All sets of the experimental data in this study are obtained by using a pressure transducer and visualized by a video camera for different water discharges (20, 25, 35 and 45 l/min), different air discharges (10, 20, 30 and 40 l/min) and different angle of attack (0, 15 and 30 degree). While the numerical simulation is conducted by using commercial Fluent CFD software to investigate the steady and unsteady turbulent two dimensional flows for different air and water velocities. The results show that when the angle of attack increases at constant air and water discharge or when air discharge increases with constant water discharge and angle of attack or when water discharge increases with constant air discharge and angle of attack, the pressure difference increases at the inlet and the outlet of the rectangular channel.

**KEYWORDS:** experimental study, Fluent CFD software investigation, two-phase flow phenomena, straight hydrofoil, enlarging channel

## I. INTRODUCTION

It is not possible to understand the two-phase flow phenomena without a clear understanding of the flow patterns encountered. It is expected that the flow patterns will influence the two -phase pressure drop, holdup, system stability, exchange rates of moment um, heat and mass during the phase-change heat transfer processes. The ability to accurately predict the type of flow is necessary before relevant calculation techniques can be developed [1]. The flow patterns of gas-liquid two-phase flow could be bubble flow, slug flow, plug flow, stratified flow, wavy flow and disperse flow. There are still many challenges associated with a fundamental understanding of flow patterns in multiphase flow and considerable research is necessary before reliable design tools become available. Gas-liquid flow was extensively used in industrial systems such as power generation units, cooling and heating systems (i.e. heat exchangers and manifolds), safety valves, etc. Thus two-phase flow characteristics through these singularities should be identified in order to be used in designing of the system [2]. In the last decade, the stratified flows are increasingly modeled with computational fluid dynamics (CFD) codes. In CFD, closure models are required that must be validated. The recent improvements of the multiphase flow modeling in the ANSYS code make it now possible to simulate these mechanisms in detail [3]. A comprehensive treatment of all sources of pressure drop within intermittent gas-liquid flows was presented [4]. Pressure loss associated with the viscous dissipation within a slug was calculated, and the presence of dispersed bubbles in a slug was accounted for, without recourse to the widely used assumption of homogenous flow. Experiments were conducted to measure pressure gradient within two air-water pipes of 32 and 50 mm internal diameter at 0 and +10° inclination to the horizontal. The results show that existing intermittent flow models predict pressure gradients considerably lower than were observed. The model predicted pressure gradients in good agreement with all the measurements and this was achieved without introducing any additional reliance on empirical information. The scope of a numerical-experimental collaborative research program, whose main objective was to understand the mechanisms of instabilities in partial cavitating flow, was carried out [5]. Experiments were conducted in the configuration of a rectangular foil located in a cavitation tunnel. Partial cavitation was investigated by multipoint

wall-pressure measurements together with lift and drag measurements and numerical videos. The algorithm of resolution was derived from the SIMPLE approach, modified to take into account the high compressibility of the medium. Three-dimensional unsteady cavitating flow around a NACA0015 hydrofoil fixed between the sidewalls was simulated [6] and the mechanism of U-shaped cloud cavity formation was clarified. A local homogeneous model was used for the modeling of the vapor– liquid two-phase medium. The compressible two-phase Navier–Stokes equations as the governing equations were solved. The cell-centered finite volume method was employed to discretize the governing equations. Assuming turbulent flow, the turbulent eddy viscosity coefficient was computed. As a result, even in the case of cavitating flow without sidewalls, the shed cloud cavities have slightly 3D structure, which was not so much large as extending across the whole spanwise direction. On the other hand, in the case of cavitating flow with sidewalls, the end of sheet cavities bows in the spanwise direction because of the development of boundary layer near both sidewalls. After that, due to the occurring of the reentrant jet towards the mid-span region, the sheet cavities breaks off from mid-span region near the leading edge of the hydrofoil, and became the vortical cloud cavities, which have the large-scale U-shaped structure. The two-dimensional simulation for an air-water bubbly flow around a hydrofoil was studied [7]. The vortex method, proposed by the authors for gas-liquid two-phase free turbulent flow in a prior paper, was applied for the simulation. The liquid vorticity field was discretized by vortex elements, and the behavior of vortex element and the bubble motion were simultaneously computed. The effect of bubble motion on the liquid flow was taken into account through the change in the strength of vortex element. The bubbly flow around a hydrofoil of NACA4412 with a chord length 100 mm was simulated. The Reynolds number is  $2.5 \times 10^5$ , the bubble diameter was 1 mm, and the volumetric flow ratio of bubble to whole fluid was 0.048. It was confirmed that the simulated distributions of air volume fraction and pressure agreed well with the trend of the measurement and that the effect of angle of attack on the flow was favorably analyzed. These results demonstrate that the vortex method was applicable to the bubbly flow analysis around a hydrofoil. Particle image velocimetry was used to examine the flow behind a two-dimensional heaving hydrofoil of NACA 0012 cross section [8]. The deflection angle of the wake, which was related to the average lift and drag on the hydrofoil, was found to lie between 13 and 18. An examination of the swirl strength of the vortices generated by the hydrofoil motion reveals that the strongest vortices, which were created at the higher Strouhal numbers, dissipated most rapidly.

The two-phase pressure drop in a hydrofoil-based micro pin fin heat sink has been investigated using R-123 as the working fluid [9]. Two-phase frictional multipliers have been obtained over mass fluxes from 976 to 2349 kg/m<sup>2</sup>s and liquid and gas superficial velocities from 0.38 to 1.89 m/s and from 0.19 to 24 m/s, respectively. It has been found that the two-phase frictional multiplier was strongly dependent on flow pattern. The theoretical prediction using Martinelli parameter based on the laminar fluid and laminar gas flow represented the experimental data fairly well for the spray-annular flow. For the bubbly and wavy-intermittent flow, however, large deviations from the experimental data were recorded. The Martinelli parameter was successfully used to determine the flow patterns, which were bubbly, wavy-intermittent, and spray-annular flow in that study. Cavitating flows, which can occur in a variety of practical cases, can be modeled with a wide range of methods. One strategy consists of using the RANS (Reynolds Averaged Navier Stokes) equations and an additional transport equation for the liquid volume fraction, where mass transfer rate due to cavitation is modeled by a mass transfer model. Three widespread mass transfer models for the prediction of sheet cavitation around a hydrofoil were compared [10]. These models share the common feature of employing empirical coefficients, to tune the models of condensation and evaporation processes, which can influence the accuracy and stability of the numerical predictions. In order to compare the different mass transfer models fairly and congruently, the empirical coefficients of the different models were first well-tuned using an optimization strategy. The resulting well-tuned mass transfer models are then compared considering the flow around the NACA66 (MOD) and NACA009 hydrofoils. The numerical predictions based on the three different tuned mass transfer models were very close to each other and in agreement with the experimental data. Moreover, the optimization strategy seemed to be stable and accurate, and could be extended to additional mass transfer models and further flow problems.

From the previous review it is denoted that the recent researches for the turbulent two phase bubbly flow in enlarging channel and existence of a hydrofoil with different angle of attack are very limited. So, our concern in this investigation is to study the effects of wide range of air/water discharge in the steady and unsteady cases on the flow behavior with the enlargement from the circular tube of the water phases which contains the air phase tube, to the rectangular channel with the existence of a hydrofoil. The channel allows in particular the study of air-water bubbly/wavy flow under atmospheric pressure. Parallel to the experiments,

CFD-Fluent simulations were carried out. The behavior of bubbly/wavy generation and propagation was qualitatively reproduced by the simulation.

## II. THE PHYSICAL MODEL AND EXPERIMENTAL APPARATUS

Fig.1 shows a schematic and photograph of the experimental Apparatus and measurements system. The rig is consists of, as shown in Fig. 2:

- 1- Main water tank of capacity (1 m<sup>3</sup>).
- 2- Water pump with specification quantity (0.08 m<sup>3</sup>/min) and head (8 m).
- 3- Valves and piping system (1.25 in)
- 4- Adjustable volume flow rate of range (10-80 l/min) is used to control the liquid (water) volume flow rates that enter test section.
- 5- Air compressor and it has a specification capacity of (0.5 m<sup>3</sup>) and maximum pressure of (16 bars).
- 6- Rotameter was used to control the gas (air) volume flow rates that enter the test section. It has a volume flow rate range of (6-50 l/min).
- 7- Valves and piping system (0.5 in) and gages.
- 8- Pressure transducer sensors which are used to record the pressure field with a range of (0-1 bar) and these pressure transducer sensors are located in honeycombs at the entrance and at the end of the test section. The pressure sensors with a distance of (80 cm) between each other are measuring with an accuracy of (0.1%).
- 9- The hydrofoil used is made of stainless steel and its dimensions are (3 cm) for the height and all other dimensions is given in figures (3-a & b). The hydrofoil is coated with a very thin layer of gray paint and its center located at (11.5 cm) from the entrance of the test section.
- 10- The test section is consisting of rectangular channel and a hydrofoil. The rectangular cross sectional area is (10 cm × 3 cm) and has length of (70 cm) which is used to show the behavior of the two phase flow around the hydrofoil and to measure the pressure difference and records this behavior. The hydrofoil is mounted and fixed by screw and nut on a blind panel on the bottom of the rectangular channel. The three large Perspex windows of the channel (two lateral sides with lighting and the top side) allowing optical access through the test section. Two enlargement connecting parts are made of steel and manufactured with smooth slope. The first one is used to connect the test section with the outside water pipe in the entrance side while the second one is used to connect the test section with the outside mixture pipe in the exit side. The inside air pipe, in the entrance side, is holed and contained inside the water pipe by a steel flange.
- 11- Interface system consists of two parts which are the data logger and the transformer which contains in a plastic box. The data logger has a three connections two of them are connected to the outside of the box (one connected to the sensors and the other connected to the personal computer), the third connection is connected to the transformer, which is work to receive the signals as a voltage from the sensors and transmit it into the transformer and then re-received these signals after converting it to ampere signals in the transformer.
- 12- The interface system which is connected with a personal computer so that the measured pressure across the test section is displayed directly on the computer screen by using a suitable program.
- 13- A Sony digital video camera recorder of DCR-SR68E model of capacity 80 GB with lens of Carl Zeiss Vario-Tessar of 60 x optical, 2000 x digital is used to visualize the flow structure. The visualized data are analyzed by using a AVS video convertor software version 8.1. A typical sequence snapshots recorded by the camera using a recording rate of 30 f/s.

The flows of both gas and liquid are regulated respectively by the combination of valves and by-passages before they are measured by gas phase flow meter and liquid phase flow meter. The gas phase and the liquid phase are mixed in the enlargement connection part before they enter the test section. When the two-phase mixture flows out of the test section, the liquid phase and the gas phase are separated in liquid storage tank. Experiments were carried out to show the effect of different operation conditions on pressure difference across the test section and to visualize the flow around the hydrofoil. These conditions are water discharges, air discharges and angles of attack. The selected experimental values for water discharges are (20, 25, 35 and 45 l/min), for air discharges are (10, 20, 30 and 40 l/min) and for angles of attack are (0°, 15°, 30°).

The experimental procedures are:

- 1- Fix the hydrofoil at the channel bottom side at the first value of angle of attack (0°).
- 2- Turn on the water pump at the first value (20 l/min).
- 3- Turn on the air compressor at the first value (10 l/min).
- 4- Record the pressure drop through the test section and photograph the motion of the two-phase flow by the digital camera.

- 5- Repeat steps (2 to 5) after changing the water discharge.
  - 6- Repeat step (5) after changing the air discharge.
  - 7- Repeat the above steps after changing the hydrofoil angle of attack.
- These give sixteen (16) experimental cases for volume fraction (Air/Water ratios) for each angle of attack.

### III. Numerical Modeling

In this study, the computational fluid dynamics (CFD) software have been applied for the numerical simulation for adiabatic gas-liquid flow characteristics through a horizontal channel contain a hydrofoil (different angle of attack every time) with smooth expansion from the liquid pipe in steady and unsteady cases for 2D. In order to compare numerical results with experimental ones, air-water couple has been selected as the representative of the gas-liquid two-phase flow. Construction of the numerical domain and the analysis are performed via GAMBIT and FLUENT (ANSYS 13.0) CFD codes, respectively. Two-phase flow variables such as void fraction and flow velocity for liquid (water) and gas (air) at the inlet condition, and the geometrical values of the system (i.e. channel length, width and height, pipes and inlet enlargement connecting part dimensions, and hydrofoil angle of attack) used in the analysis are selected as the same variables as the experimental part. Atmospheric conditions are valid for the experimental facility. Total test rig length in the experiments, thus in the numerical domain, is (100 cm) including (70 cm) for the test section containing the obstacle, and (30 cm) for the inlet enlargement part. Water pipe diameter is (3.175 cm) and air pipe diameter is (1.27 cm) as shown in Fig. 4. The 2D physical model is established using a model of flow focusing channel in CFD. The enlargement connecting part length consists of: (0.05 m) circular pipe, (0.15 m) diverge-link to change the shape from circular to rectangular and (0.1 m) rectangular duct. Air and water are selected to be working fluids and their fluid properties are in Table 1.

**Table 1 Property parameters of the gas and liquid in CFD.**

Fluid	Density (kg/m <sup>3</sup> )	Viscosity (kg/m.s)	Surface Tension
Water	998.2	$10.03 \times 10^{-04}$	0.072
Air	1.225	$1.7894 \times 10^{-05}$	---

The model geometry structure was meshed by the preprocessor software of GAMBIT with the Quad/Pave grids. After meshing, the model contained (2D) 23009 grid nodes for 0° angle of attack (23154 for 15° and 23218 for 30°), 22433 cells for 0° angle of attack (22578 for 15° and 22642 for 30°) and 44290 faces for 0° angle of attack (44290 for 15° and 44708 for 30°) -as demonstrated in Fig. 4 for 15° angle of attack- before importing into the processor Fluent for calculation. This refinement grid provided a precise solution to capture the complex flow field around the hydrofoil and mixing region in the enlargement connecting part. The boundary conditions are the velocity inlet to the air and water feeding (Table 2) and the pressure outlet to the model outlet. In Fluent, the Mixture Multiphase model was adopted to simulate the flow. The mixture model is a simplified Eulerian approach for modeling *n*-phase flows [11]. Because the flow rates of the air and water in the channel are high, the turbulent model (*k-ε* Standard Wall Function) has been selected for calculation. The other options in Fluent are selected: SIMPLE (Semi-Implicit Method for Pressure-Linked Equations) scheme for the pressure-velocity coupling, PRESTO (pressure staggering option) scheme for the pressure interpolation, Green-Gauss Cell Based option for gradients, First-order Up-wind Differencing scheme for the momentum equation, the schiller-naumann scheme for the drag coefficient, manninen-et-al for the slip velocity and other selections are described in Table 3. The time step (for unsteady case), maximum number of iteration and relaxation factors have been selected with proper values to enable convergence for solution which is about to (0.001) for all parameters.

**Table 2 Air-water flow cases.**

Case number	Air/water discharges (l/min)	Air/water velocities (m/sec)	Case number	Air/water discharge (l/min)	Air/water velocities (m/sec)
1	10/20	1.32/0.50	5	20/20	2.63/0.50
2	10/25	1.32/0.63	6	20/25	2.63/0.63
3	10/35	1.32/0.87	7	20/35	2.63/0.87
4	10/45	1.32/1.12	8	20/45	2.63/1.12
Case number	Air/water discharge (l/min)	Air/water velocities (m/sec)	Case number	Air/water discharge (l/min)	Air/water velocities

					(m/sec)
9	30/20	3.95/0.50	13	40/20	5.26/0.50
10	30/25	3.95/0.63	14	40/25	5.26/0.63
11	30/35	3.95/0.87	15	40/35	5.26/0.87
12	30/45	3.95/1.12	16	40/45	5.26/1.12

Table 3 Other mixture model selections for Fluent.

Solver type	$k-\varepsilon$ Model	Solution Methods
Pressure-Based	Cmu=0.09, C1-Epsilon=1.44, C2-Epsilon=1.92	Volume Fraction and Turbulent Kinetic Energy (First-order Up-wind)
Starting Solution Controls (Under-Relaxation Factors)		
Pressure=0.3, Momentum=0.7, Turbulent Kinetic Energy & Turbulent Dissipation Rate=0.8		
Specification Method for turbulence		
Turbulent Intensity (=3%) and Hydraulic Diameter = (0.0127 m, 0.0191 m and 0.1 m) for inlet air, inlet water and mixture outlet respectively		
Solution Initialization		
Turbulent Kinetic Energy ( $m^2/s^2$ )=0.0003375, Turbulent Dissipation Rate ( $m^2/s^3$ )= 0.0007620108 and air-bubble Volume Fraction=0		

The hydrodynamics of two-phase flow can be described by the equations for the conservation of mass and momentum, together with an additional advection equation to determine the gas-liquid interface. The two-phase flow is assumed to be incompressible since the pressure drop along the axis orientation is small. For the incompressible working fluids, the governing equations of the Mixture Multiphase Model are as following [11]-[12]:

- The continuity equation for the mixture is:

$$\frac{\partial}{\partial t}(\rho_m) + \nabla \cdot (\rho_m \vec{v}_m) = 0 \quad (1)$$

Where  $\vec{v}_m$  is the mass-averaged velocity:

$$\vec{v}_m = \frac{\sum_{k=1}^n \alpha_k \rho_k \vec{v}_k}{\rho_m} \quad (2)$$

and  $\rho_m$  is the mixture density:

$$\rho_m = \sum_{k=1}^n \alpha_k \rho_k \quad (3)$$

$\alpha_k$  is the volume fraction of phase  $k$ .

- The momentum equation for the mixture can be obtained by summing the individual momentum equations for all phases. It can be expressed as:

$$\frac{\partial}{\partial t}(\rho_m \vec{v}_m) + \nabla \cdot (\rho_m \vec{v}_m \vec{v}_m) = -\nabla p + \nabla \cdot [\mu_m (\nabla \vec{v}_m + \nabla \vec{v}_m^T)] + \rho_m \vec{g} + \vec{F} + \nabla \cdot (\sum_{k=1}^n \alpha_k \rho_k \vec{v}_{dr,k} \vec{v}) \quad (4)$$

where  $n$  is the number of phases,  $\vec{F}$  is a body force and  $\mu_m$  is the viscosity of the mixture:

$$\mu_m = \sum_{k=1}^n \alpha_k \mu_k \quad (5)$$

$\vec{v}_{dr,k}$  is the drift velocity for secondary phase  $k$ :

$$\vec{v}_{dr,k} = \vec{v}_k - \vec{v}_m \quad (6)$$

From the continuity equation for secondary phase  $p$ , the volume fraction equation for secondary phase  $p$  can be obtained:

$$\frac{\partial}{\partial t} (\alpha_p \rho_p) + \nabla \cdot (\alpha_p \rho_p \vec{v}_m) = -\nabla \cdot (\alpha_p \rho_p \vec{v}_{dr,p}) + \sum_{q=1}^n (\dot{m}_{qp} - \dot{m}_{pq}) \quad (7)$$

The relative velocity (also referred to as the slip velocity) is defined as the velocity of a secondary phase ( $p$ ) relative to the velocity of the primary phase ( $q$ ):

$$\vec{v}_{pq} = \vec{v}_p - \vec{v}_q \quad (8)$$

The mass fraction for any phase ( $k$ ) is defined as:

$$c_k = \frac{\alpha_k \rho_k}{\rho_m} \quad (9)$$

The drift velocity and the relative velocity ( $\vec{v}_{qp}$ ) are connected by the following expression:

$$\vec{v}_{dr,p} = \vec{v}_{pq} - \sum_{k=1}^n c_k \vec{v}_{qk} \quad (10)$$

ANSYS FLUENT's mixture model makes use of an algebraic slip formulation. The basic assumption of the algebraic slip mixture model is that to prescribe an algebraic relation for the relative velocity, a local equilibrium between the phases should be reached over a short spatial length scale. The form of the relative velocity is given by:

$$\vec{v}_{pq} = \frac{\tau_p (\rho_p - \rho_m)}{f_{drag} \rho_p} \vec{a} \quad (11)$$

where  $\tau_p$  is the particle relaxation time:

$$\tau_p = \frac{\rho_p d_p^2}{18 \mu_q} \quad (12)$$

$d$  is the diameter of the particles (or droplets or bubbles) of secondary phase  $p$ ,  $\vec{a}$  is the secondary-phase particle's acceleration. The default drag function  $f_{drag}$ :

$$f_{drag} = \begin{cases} 1 + 0.15 Re^{0.687} & Re \leq 1000 \\ 0.0183 Re & Re > 1000 \end{cases} \quad (13)$$

and the acceleration  $\vec{a}$  is of the form:

$$\vec{a} = \vec{g} - (\vec{v}_m \cdot \nabla) \vec{v}_m - \frac{\partial \vec{v}_m}{\partial t} \quad (14)$$

The simplest algebraic slip formulation is the so-called drift flux model, in which the acceleration of the particle is given by gravity and/or a centrifugal force and the particulate relaxation time is modified to take into account the presence of other particles.

In turbulent flows the relative velocity should contain a diffusion term due to the dispersion appearing in the momentum equation for the dispersed phase. ANSYS FLUENT adds this dispersion to the relative velocity:

$$\vec{v}_{pq} = \frac{(\rho_p - \rho_m) d_p^2}{18 \mu_q f_{drag} \rho_p} \vec{a} - \frac{\eta_t}{\sigma_t} \left( \frac{\nabla \alpha_p}{\alpha_p} - \frac{\nabla \alpha_q}{\alpha_q} \right) \quad (15)$$

where  $\sigma_t$  is a Prandtl/Schmidt number set to 0.75 and  $\eta_t$  is the turbulent diffusivity. This diffusivity is calculated from the continuous-dispersed fluctuating velocity correlation, such that:

$$\eta_t = C_\mu \frac{k^2}{\varepsilon} \left( \frac{\gamma_y}{1 + \gamma_y} \right) \left( 1 + C_\beta \frac{\varepsilon^2}{\gamma_y} \right)^{-1/2} \quad (16)$$

$$\frac{\varepsilon}{\gamma_y} = \frac{|\vec{v}_{pq}|}{\sqrt{2/3} k} \quad (17)$$

Where  $C_\beta = 1.8 - 1.35 \cos^2 \theta$ ,  $\cos \theta = \frac{\vec{v}_{pq} \cdot \vec{v}_p}{|\vec{v}_{pq}| |\vec{v}_p|}$  and  $\gamma_y$  is the time ratio between the time scale of the energetic turbulent eddies affected by the crossing-trajectories effect and the particle relaxation time. If the slip velocity is not solved, the mixture model is reduced to a homogeneous multiphase model. In FLUENT application, boundary conditions like "velocity inlet" is taken as the inlet condition for water and air while "interior" and "outflow" are employed as the water-air mixture. Air is injected to the water via an air pipe in the experiments, therefore, the gas flow through the air pipe and the mixture occurred outlet of it are modeled in 3D. According to the simulation, air with known mass flow rate flows through air pipe and then disperses into the water at the exit of the pipe. At air flow rates (thus volumetric void fraction), phase inlet velocity and void fraction profiles obtained at the air and water pipes outlet are extracted from the experimental calculations in order to be introduced as the inlet condition for the flow analysis regarding the numerical 2D domain. In the present study bubble diameter is equal to (1 cm). Assuming the bubbles are in spherical shape and neglecting the coalescence between them along the channel.

#### IV. EXPERIMENTAL RESULTS

The experimental results are represent the gas-liquid flow through channel with the existence of the hydrofoil for different water discharges (20, 25, 35 and 45 l/min), different air discharge (10, 20, 30 and 40 l/min) and different angle of attack ( $0^\circ$ ,  $15^\circ$  and  $30^\circ$ ) as photographs and pressure graphs. Below are some of these cases.

#### **4.1. Effect of Air and Water Discharges**

Figs (5 and 6) show photographs for the two phase flow behavior around the hydrofoil of water discharge ( $Q_w=20$  and  $25$  l/min) respectively and air discharges ( $Q_a =$  (a)10, (b)20, (c)30 and (d)40 l/min) for the three angles of attack ( $0^\circ$ ,  $15^\circ$  and  $30^\circ$ ) from top to bottom. It shows that the number (amount) of bubble is few and has small size at low water discharge. These photographs describe the flow behavior and it appears that it is near to slug region when the discharge is low. This is due to the low velocity of water at low water discharge. Also when increase the air discharge the size and number of bubbles increases and the bubble cavities develops to cloud cavitations especially at high air discharge. This is due to the high velocity of water at high water discharge which leads to more turbulence in the flow and the flow becomes bubbly as shown. It is clear that the flow becomes unstable and unsymmetrical around the hydrofoil and the number and size of bubble becomes higher compared with the low velocities cases. It appears that the vortices behind and beside the hydrofoil becomes more strong compared with the low discharge cases. When the two phases increases, more unsteady behavior is noticed and the flow oscillates between bubble and disperse regions. Also, when water discharge increases with increase air discharge, flow becomes unsteady, vortices developed around the hydrofoil surface and most bubbles transformed to cloudy flow, then a disperse region and strong vortex shedding is observed. This is due to the important effect of the hydrofoil existence in the rectangular channel which effect on pressure difference across the inlet and outlet of the channel. The experimental data shows that the average number of bubbles generally increases with increasing mixture velocities. Independently of the inlet velocities, the highest number of bubbles is found in the mixing region. Moreover, higher gas velocities have a higher number of bubbles in the mixing region.

#### **4.2. Effect of Angle of Attack**

Figures (7, 8, 9, 10, 11 and 12) show photographs for the two phase flow behavior around the hydrofoil of water discharges ( $Q_w=35$  and  $45$  l/min) respectively and air discharges ( $Q_a=$  (a)10, (b)20, (c)30 and (d)40 l/min) from top to bottom for different values of angles of attack for the straight hydrofoil ( $0^\circ$ ,  $15^\circ$  and  $30^\circ$ ). These figures show that the number and size of bubbles increases and cavities become larger when the angle of attack increases at constant air and water discharge and the flow becomes unstable behind and beside the straight hydrofoil. Also the increase in the angle of attack leads to the vortex generation, the flow becomes unsteady and asymmetric around and behind the straight hydrofoil and most bubbles cavity develop to cloud cavities.

#### **4.3. Pressure Difference**

Figures (13 and 14) represent the mean pressure difference with air discharge for different values of water discharge for the three angles of attack. When air or water discharge increases, the mean pressure difference increases. This is due to the increase of air or water discharge resulting in velocity increases. Also, the mean pressure difference has a significant influence on two-phase flow behavior. Therefore, it is expected that the flow instability will also depend upon the pressure difference. Moreover when the air discharge increases, the pressure fluctuation increases. This is due to the high inertia force in the two phase flow. At these angles of attack, the increase in air and water discharges resulting in pressure difference increasing. This is due to the transition from laminar to turbulent boundary layer, therefore the pressure difference increases.

#### **4.4. Time Evolution of Pressure**

Figure 15 represents the effect of time evolution of pressure for different angle of attack, air and water discharges obtained by experiments. The pressure sensor at the inlet and outlet of the test section are record pressures that fluctuating as a function of time due to two-phase flow effect. At the same air and water discharge the increase in the angle of attack increasing the pressures fluctuation. Also, at the same angle of attack the increase in the air and water discharge increasing the pressures fluctuation.

## **V. NUMERICAL RESULTS**

The numerical results are represented as colored contours for the same air-water discharges cases in the experimental part. As mentioned above, the 2D inlet (line) air or water velocities are calculated from the 3D experimental inlet (surface) area for the air or water discharge. These give thirty-two (32) numerical cases for volume fraction (Air/Water ratios) at each angle of attack including steady and unsteady states. In the present calculations the air–water mixture of any finite bubbles existing in each control volume is approximated to those

of infinite number of infinitesimal bubbles. Thus, the local mixture condition in the air–water two-phase medium is specified in each computational cell having the same void fraction. Below are some of these cases.

### 5.1. Steady State

Fig.s (16-a, b, c and d) depict volume fraction (water) contours for selected cases (case1, 2, 6 and 10) respectively for angle of attack ( $0^\circ$ ). While Fig.s (17-a, b, c and d) depict volume fraction contours for other selected cases (case3, 11, 12 and 16) respectively for angle of attack ( $15^\circ$ ). Also, Fig.s (18-a, b, c and d) depict volume fraction (water) contours for selected cases (case4, 7, 9 and 13) respectively for angle of attack ( $30^\circ$ ). The differences between the experimental snapshots and numerical figures are due to two reasons; the first is the differences in the overall flow rates of air and water for the same inlet velocities from the inlet regions (small lines in 2D numerical cases and big square and annulus areas in 3D experimental cases), and the second reason is that the snapshots are taken roughly from the experimental movies for each case and may be for another snapshot from the same case movie, the differences will be less. From these figures it is appear that a slug to disperse/bubbly regions flow pattern is achieved. The flow rates of air and water have a large range and it show the increase in water phase and with the decrease of the gas flow rate, the volume fraction of the gas decreased and the volume fraction of the water increased simultaneously. According to these figures, stratified water-air mixture enters the singularity section and begins to decelerate due to the smoothly enlarging cross-section and it show how the volume fraction affected the flow behavior. A uniform dispersed two-phase flow, in which the dispersed phase (either air bubbles) moves with their carrier fluid (water), approaches to the hydrofoil. Due to strong changes of both magnitude and direction of local velocities of the fluid flow (i.e. local fluid velocity gradients) and density difference between the dispersed phase and the fluid, the local phase distribution pattern changes markedly around the hydrofoil. Strong air flows are induced and a strong vortex is created as a result of the entered air and small vortices are also produced. A recirculation zone in the wake, a flow separation at the edge of the hydrofoil and a wavy motion are noticed. It is appear that maximum turbulent viscosity and high turbulence regions depends on the volume fraction ratio. Also, when air velocity increases, separation area is detected after the hydrofoil.

### 5.2. Unsteady State

Fig.s (19-a, b, c and d) represent volume fraction (water) contours development for selected unsteady case5 for angle of attack ( $0^\circ$ ). Fig.s (20-a, b, c, and d) represent volume fraction (water) contours development for unsteady case14 for angle of attack ( $15^\circ$ ). Fig.s (21-a, b, c and d) represent volume fraction (water) contours development for unsteady case8 for angle of attack ( $30^\circ$ ). Also, fig.s (22-a, b, c and d) represent volume fraction (water) contours development for unsteady case15 for angle of attack ( $30^\circ$ ). It show how the volume fraction develops with time. As can be seen, the cavitating flow behind the foil is achieved in two regions. The increase in the angle of attack leads to a cavity flow and the flow becomes unsteady behind the straight hydrofoil and most bubbles cavity develops to cloud cavities.

## VI. CONCLUSIONS

The partial cavitating flow and resulting cloud cavitation around a two-dimensional hydrofoil was investigated in this study both numerically and experimentally. The computations were performed in the configuration of the 2D hydrofoil section. This study consists of a theoretical part of a more general nature and an experimental part highlighting bubbly flows around a hydrofoil in horizontal channel. The numerical results were more closely investigated to explain the different behaviors obtained at the three angles of attack. Concluding remarks are summarized below:

- 1- Three different flow patterns are detected in flow visualization study, which are bubbly, wavy-intermittent, and spray flow patterns.
- 2- In the wavy-intermittent flow pattern, a thick liquid layer is present around the hydrofoil surface, and the air phase core and liquid layer are separated by a wavy interface.
- 3- When air discharge increases, high turbulence is appear which generate more bubbles and waves.
- 4- The pressure sensor at the inlet and outlet of the test section are record pressures that fluctuating as a function of time due to two-phase effect. Also, when air or water discharge increases, the mean pressure difference increases.
- 5- Due to strong changes of both magnitude and direction of local velocities of the fluid flow and density difference between the dispersed phase and the fluid, the local phase distribution pattern changes markedly around the hydrofoil.
- 6- It should be noted that the prediction on the bubble size does not correctly describe the size observed in experiments. This is due to the difference in the numerical definition of vapor bubble and visual bubble boundary.

- 7- In a water slug, bubbles move slower than the liquid. The average velocity of the bubbles is slightly slower than the slug tail velocity. This means that the dispersed bubbles in the liquid slug will be caught up by the arriving elongated bubble.
- 8- Realistic bubble trajectories, with a number of bubble trajectories entering the wake of a hydrofoil, are only obtained if the effect of liquid velocity fluctuations (or turbulence in the liquid) is simulated and some kind of sliding phenomenon for colliding bubbles is taken into account.
- 9- The effect of the existence of a hydrofoil is clear in dividing the two-phase flow, generate vortices and finally enhance mixing and the smooth obstacle (hydrofoil) generates less bubble and turbulence.

In this study, diameter of the bubbles is considered constant and coalescence between the bubbles is neglected. However, bubbles in the actual flow break down and unite as the flow develops along the channel and this gives a varying diameter distribution which causes lift and drag forces to be calculated locally. Therefore, a simulation considering the effects of differing bubble diameter and interfacial forces is suggested for better modeling of the flow investigated.

## REFERENCES

- [1] Brennen and Christopher Earls, "Flow Pattern, Pressure Drop and Void Fraction of Two-Phase Gas-Liquid flow In an Inclined Narrow Annular Channel", *Experimental Thermal and Fluid Science* (30), 345–354, 2006.
- [2] Brennen and Christopher Earls, "Fundamentals of Multiphase Flow", Cambridge University Press. ISBN 13 978-0-521-84804-6, 2005.
- [3] Thomas HÖHNE, "Experiments and Numerical Simulations of Horizontal Two Phase Flow Regimes", Seventh International Conference on CFD in the Minerals and Process Industries, CSIRO, Melbourne, Australia, December 2009.
- [4] E. Krepper, P. Ruyer, M. Beyer, D. Lucas, H.-M. Prasser and N. Seiler "CFD Simulation of Polydispersed Bubbly Two-Phase Flow around an Obstacle", *Science and Technology of Nuclear Installations* 239, 2372–2381, 2009.
- [5] Jean-Baptiste Leroux, Olivier Coutier-Delgosha and Jacques André Astolfi, "A Joint Experimental and Numerical Study of Mechanisms Associated to Instability of Partial Cavitation on Two-Dimensional Hydrofoil", *PHYSICS OF FLUIDS*, American Institute of Physics, 17, 052101, 2005.
- [6] Yoshinori Saito, Rieko Takami, Ichiro Nakamori and Toshiaki Ikohagi, "Numerical Analysis of Unsteady Behavior of Cloud Cavitation around a NACA0015 Foil", *Comput Mech* (2007) 40:85–96, Springer-Verlag.
- [7] Tomomi Uchiyama and Tomohiro Degawa, "Vortex Simulation of the Bubbly Flow around a Hydrofoil", *International Journal of Rotating Machinery*, Hindawi Publishing Corporation, Volume 2007.
- [8] K. D. von Ellenrieder and S. Pothos, "PIV Measurements of the Asymmetric Wake of a Two Dimensional Heaving Hydrofoil", *Exp Fluids* (2008) 44:733–745, Springer-Verlag.
- [9] Ali Koşar, "Two-Phase Pressure Drop across a Hydrofoil-Based Micro Pin Device Using R-123", *Experimental Thermal and Fluid Science* 32 (2008) 1213–1221, Scencedirect, Elsevier.
- [10] Mitja Morgut, Enrico Nobile and Ignacijo Biluš, "Comparison of Mass Transfer Models for the Numerical Prediction of Sheet Cavitation around a Hydrofoil", *International Journal of Multiphase Flow* 37 (2011) 620–626, Scencedirect, Elsevier.
- [11] Introductory FLUENT Notes, FLUENT v6.3, Fluent User Services Center, December 2006.
- [12] ANSYS 13.0 Help, FLUENT Theory Guide, Mixture Multiphase Model.
- [13] Esam M. Abed and Riyadh S. Al-Turaihi, "Experimental Study of Two-Phase Flow around Hydrofoil in Open Channel", *Journal for Mechanical and Materials Engineering*, Iraq, 2012, accepted and submitted for publication.
- [14] Riyadh S. Al-Turaihi, "Experimental Investigation of Two-Phase Flow (Gas –Liquid) around a Straight Hydrofoil in Rectangular Channel", *Journal of Babylon University*, Iraq, 2012, accepted and submitted for publication.

## Nomenclature

$c_k$	Mass fraction (-)	
$d$	Diameter of the particles	(m)
$F$	Body force	(N)
$f_{drag}$	Drag function	(-)
$g$	Gravity acceleration	(m/s <sup>2</sup> )
$\dot{m}$	Mass flow rate	(kg/m <sup>3</sup> .s)
$n$	Number of phases	(-)
$Q$	Discharge	(l/min)
$t$	Time	(sec)

## Greek Symbols

$\alpha_k$	Volume fraction of phase $k$	(-)
$\vec{a}$	Secondary-phase particle's acceleration	(m/s <sup>2</sup> )
	Turbulent diffusivity	(N/m <sup>2</sup> .s)
$\rho_m$	Mixture density	(kg/m <sup>3</sup> )

- $\tau_p$  Prandtl/Schmidt number (-)
- $\tau_p$  Particle relaxation time (sec)
- $v_m$  Mass-averaged velocity (-)
- $\vec{v}_{dr,k}$  Drift velocity for secondary phase  $k$  (velocity of an algebraic slip component relative to the mixture) (-)
- $\mu_m$  Viscosity of the mixture (N/m<sup>2</sup>.s)

Subscripts

- a Air
- $k,p$  Secondary phase
- $m$  Mixture
- w Water

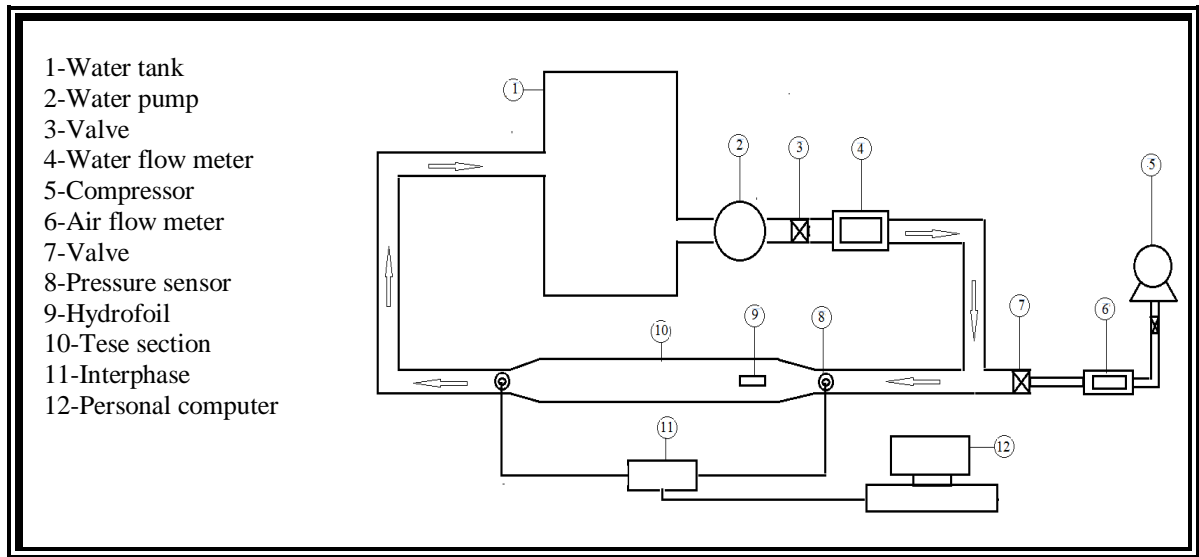


Figure 1. The experimental rig and measurements system [13]-[14].



Figure 2. (a) Water system, (b) Air flow meter, (c) Enlargement connecting part, flange, piping system and pressure transducer sensor [13]-[14].

Symbol	Dimension in(mm)	Symbol	Dimension in(mm)
A	50	D	20
B	26	E	10
C	20	F	5



Figure 3. The straight hydrofoil dimensions (mm) [14].

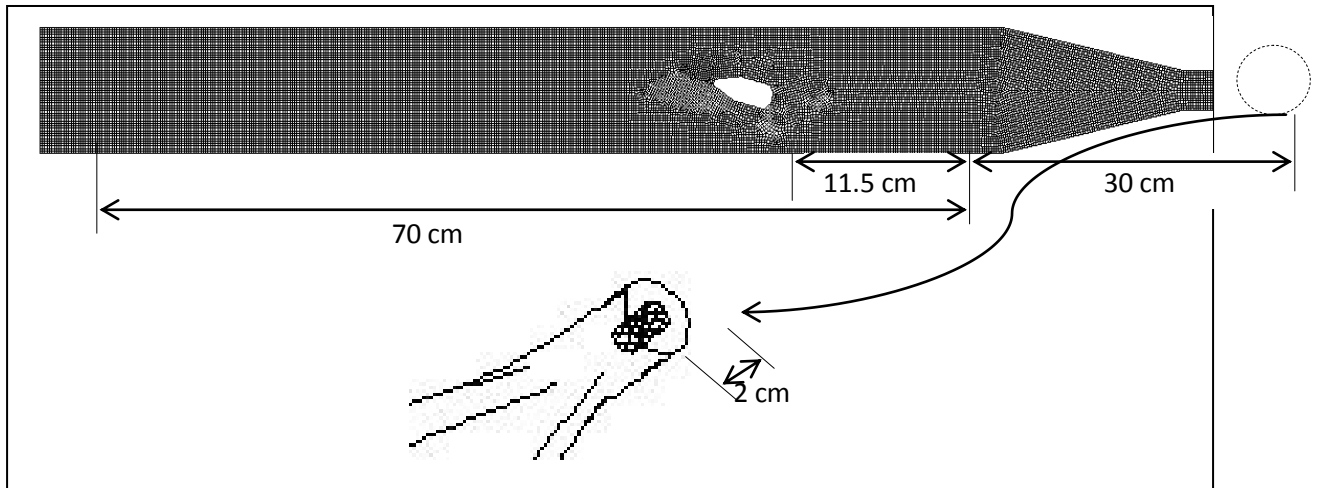


Figure 4. 2D model geometry structure mesh.

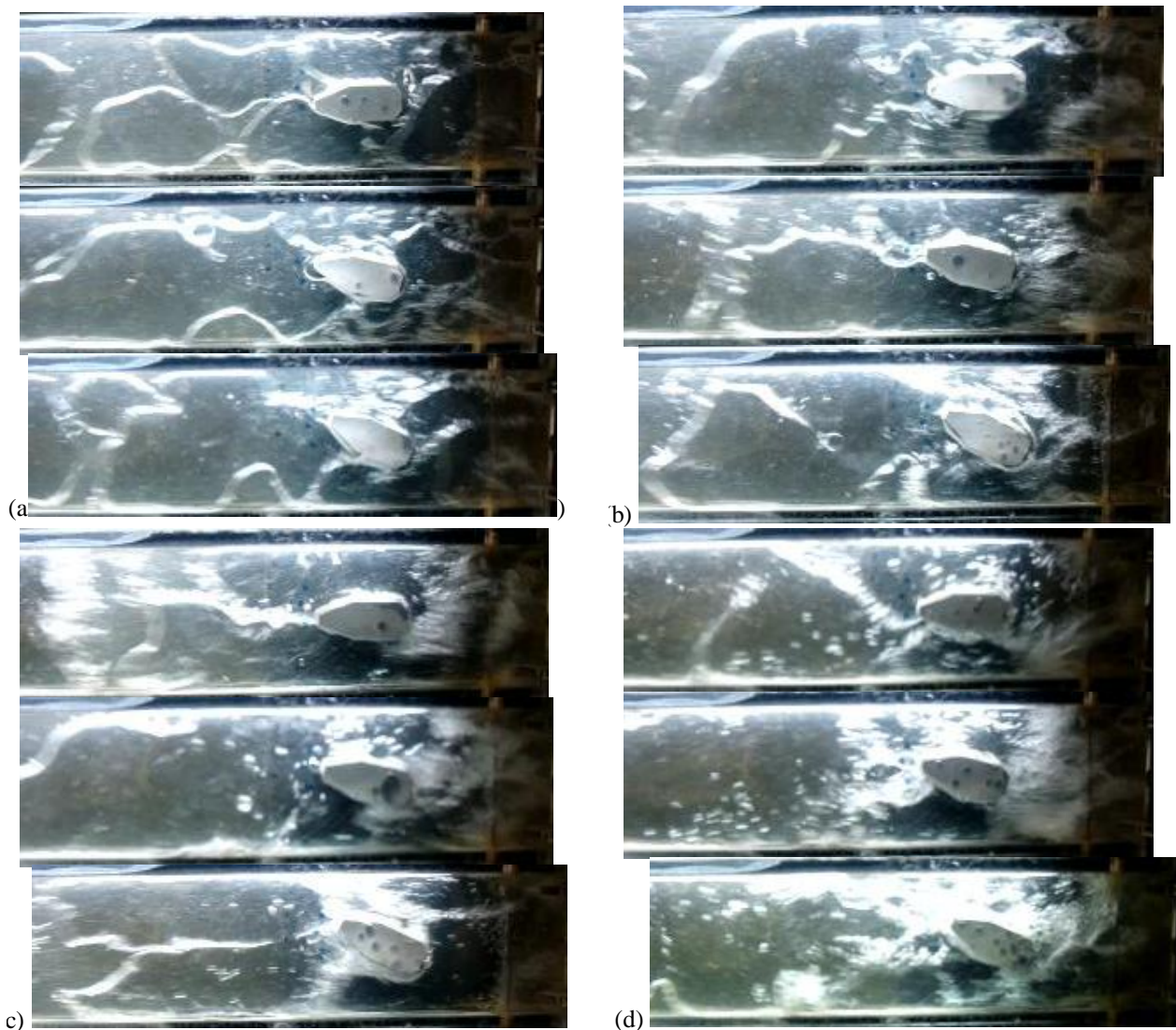


Figure 5. Photographs for the two phase flow behavior at  $Q_w=20$  l/min,  $Q_a=10, 20, 30, 40$  l/min and angle of attack= 0, 15, 30 degree respectively.

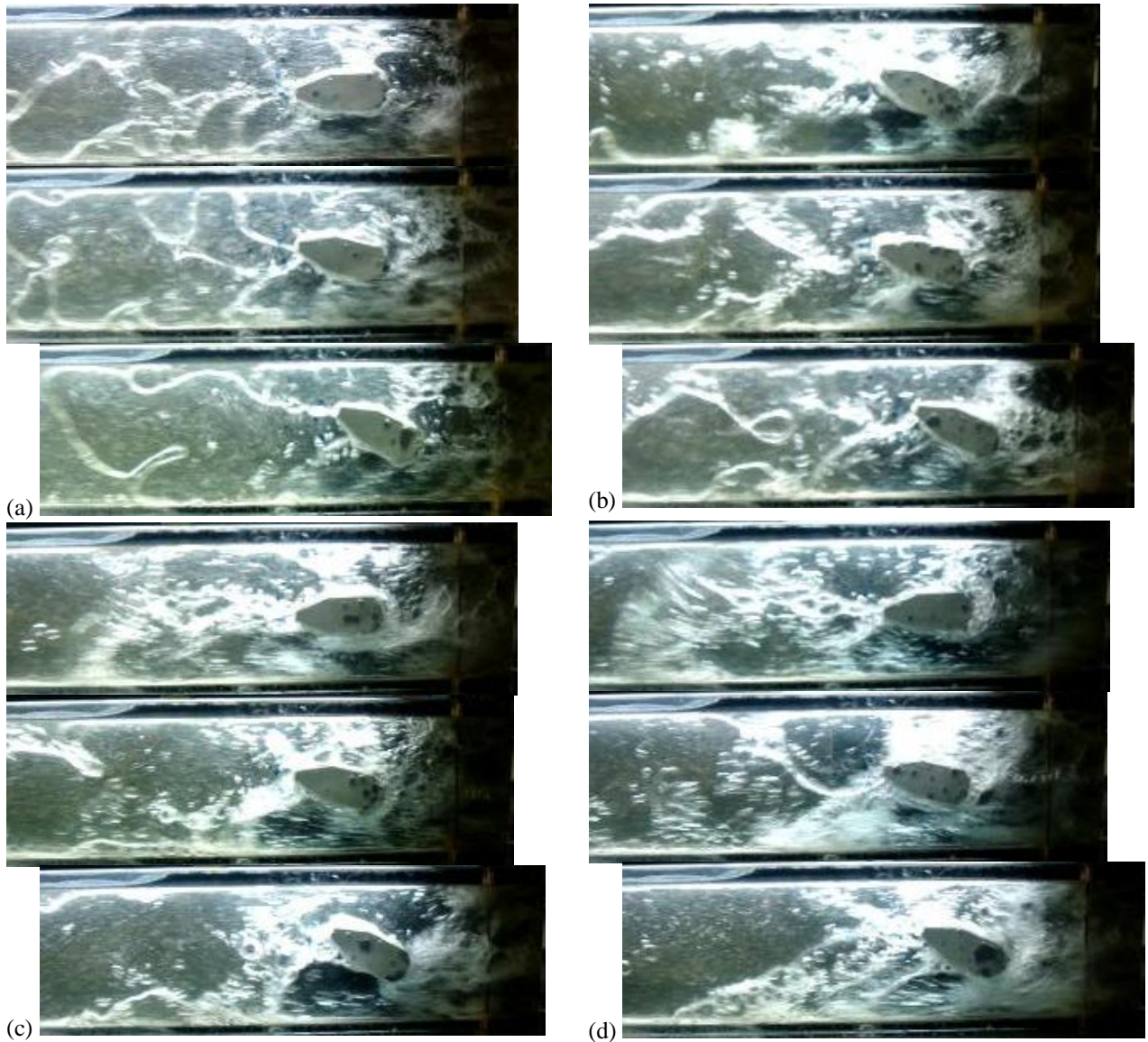


Figure 6. Photographs for the two phase flow behavior at  $Q_w=25$  l/min,  $Q_a=10, 20, 30, 40$  l/min and angle of attack= 0, 15, 30 degree respectively.

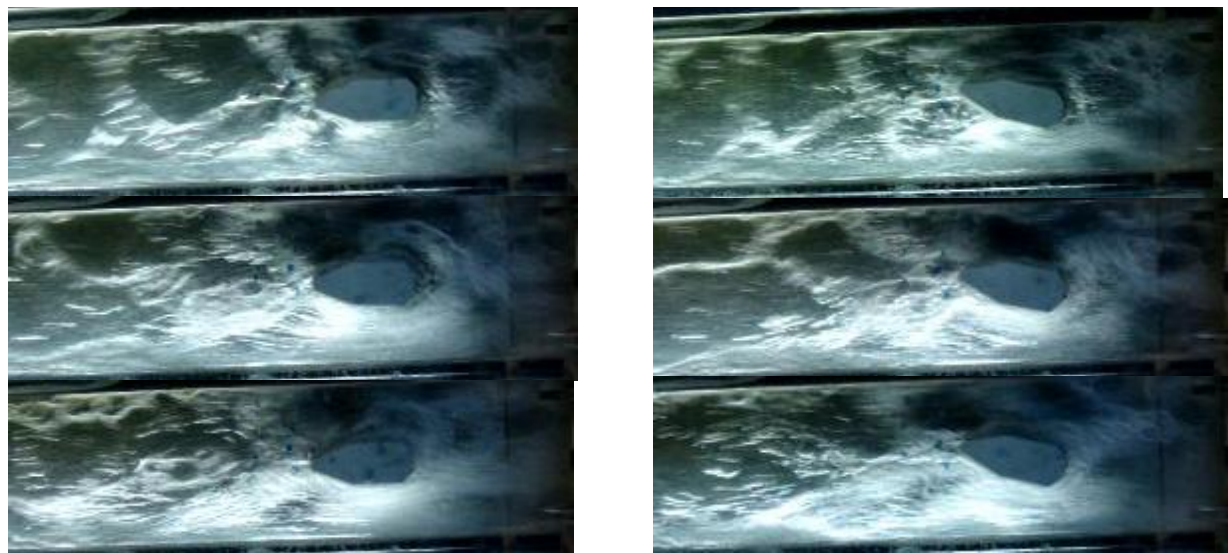




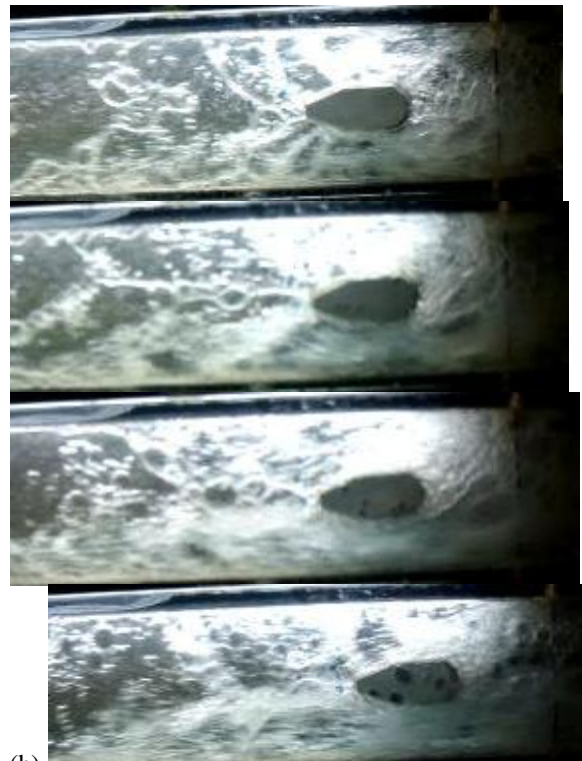
Figure 7. Photographs for the two phase flow behavior at  $Q_w=35$  l/min, angle of attack= 0 degree and  $Q_a=10, 20, 30, 40$  l/min respectively.



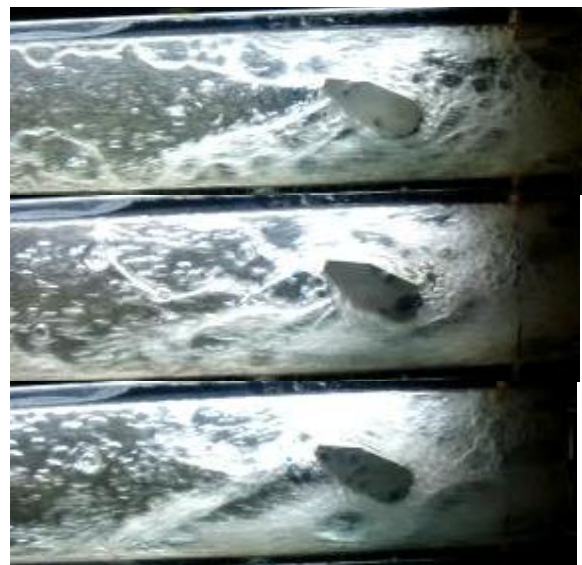
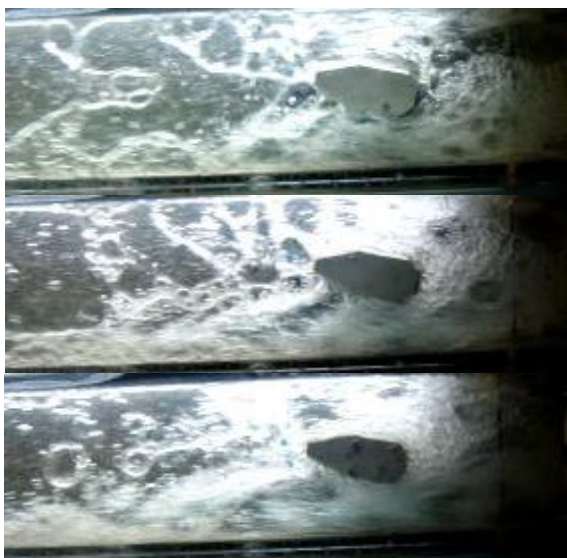
Figure 8. Photographs for the two phase flow behavior at  $Q_w=35$  l/min, angle of attack= 15 degree and  $Q_a=10, 20, 30, 40$  l/min respectively.



(a) Figure 9. Photographs for the two phase flow behavior at  $Q_w=35$  l/min, angle of attack= 30 degree and  $Q_a=10, 20, 30, 40$  l/min respectively.



(b) Figure 10. Photographs for the two phase flow behavior at  $Q_w=45$  l/min, angle of attack= 0 degree and  $Q_a=10, 20, 30, 40$  l/min respectively.





(c) Figure 11. Photographs for the two phase flow behavior at  $Q_w=45$  l/min, angle of attack= 15 degree and  $Q_a=10, 20, 30, 40$  l/min respectively.



(d) Figure 12. Photographs for the two phase flow behavior at  $Q_w=45$  l/min, angle of attack= 30 degree and  $Q_a=10, 20, 30, 40$  l/min respectively.

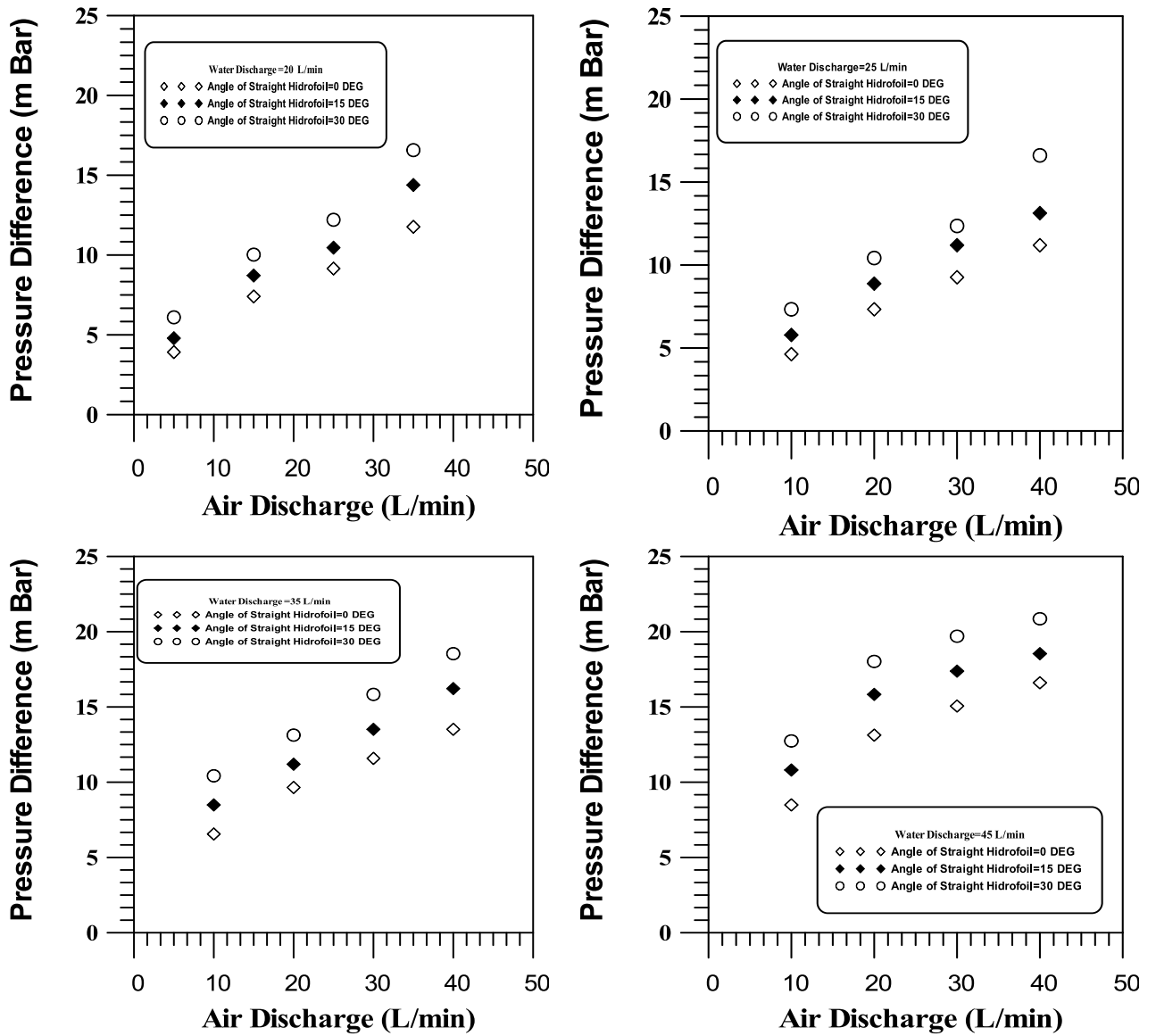


Figure 13. Mean pressure difference with air discharge for different values angle of attack.

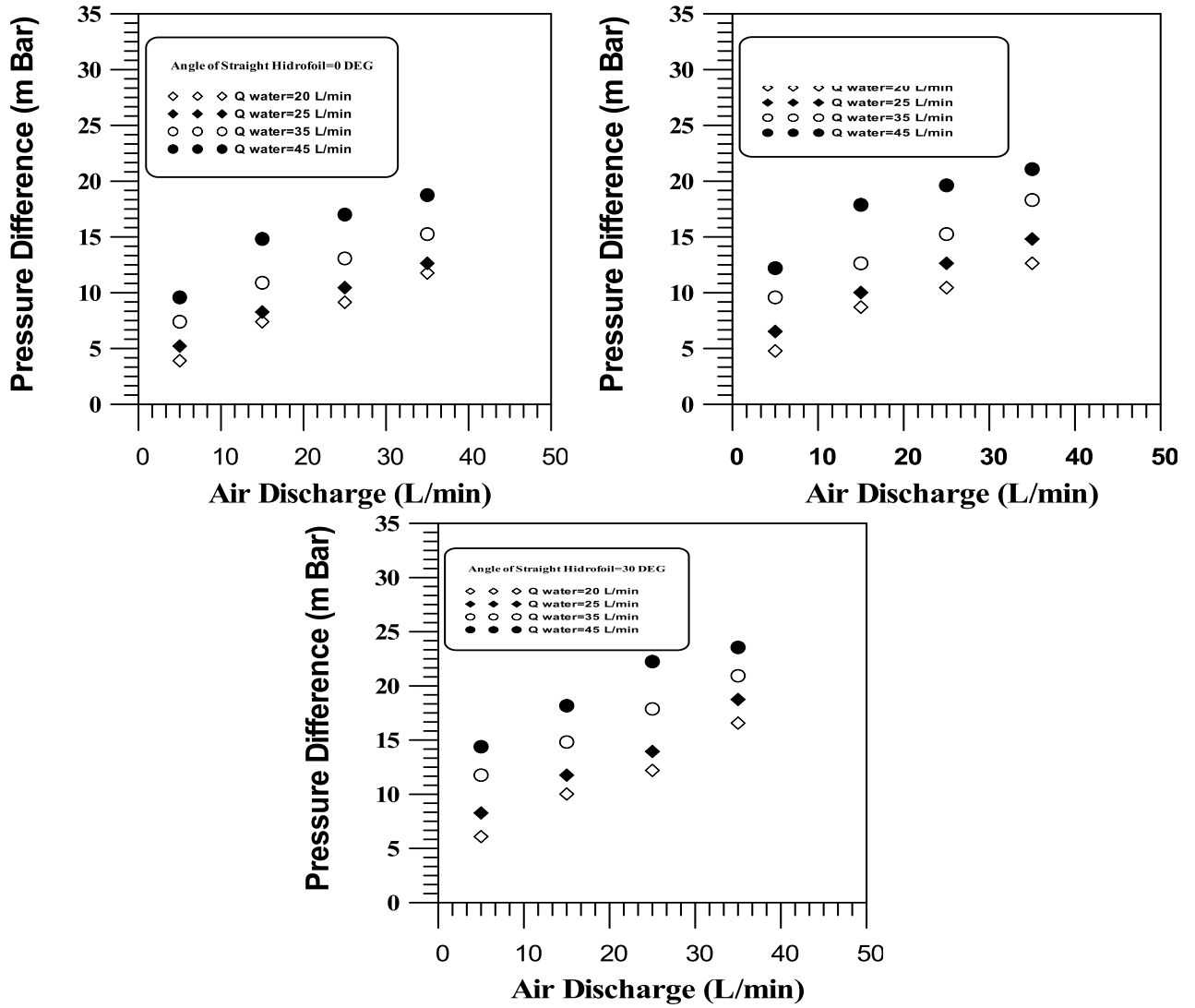
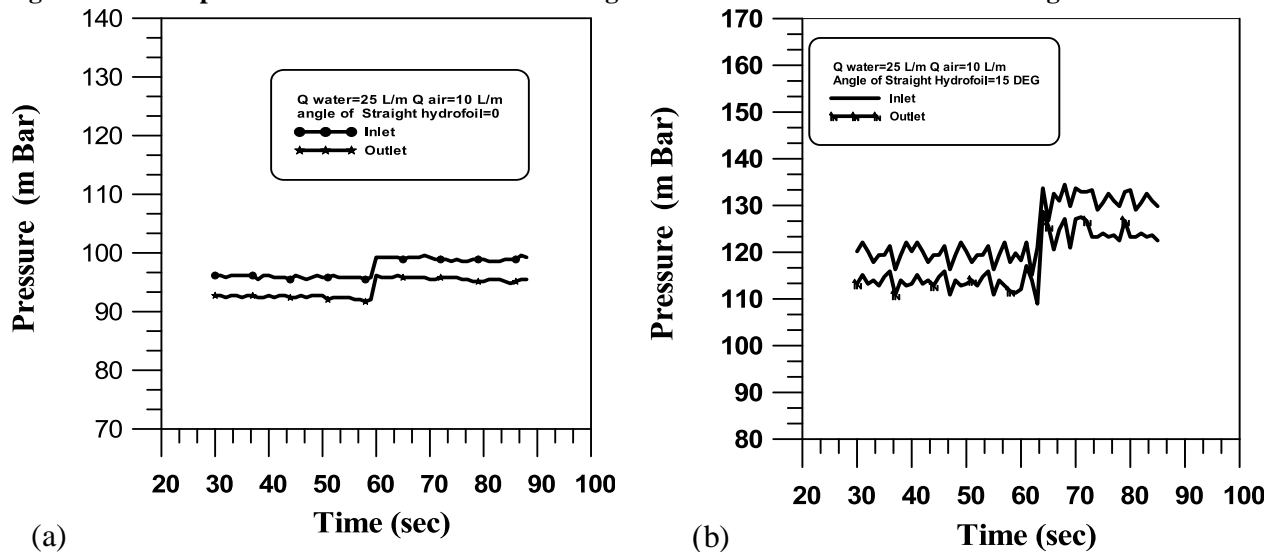


Figure 14. Mean pressure difference with air discharge for different values of water discharge.



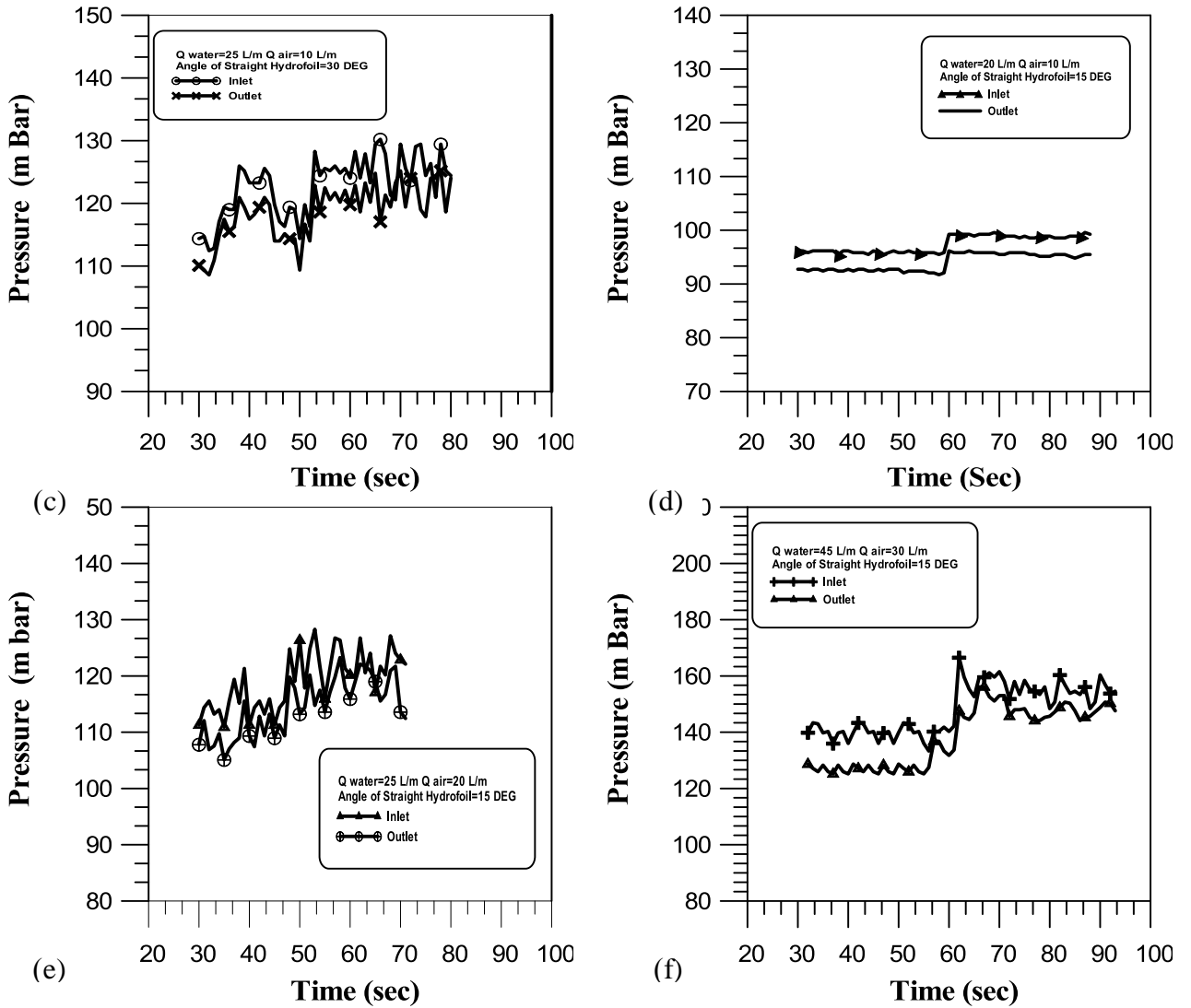


Figure 15. Effect of time evolution of pressure for different angle of attack, air and water discharges.

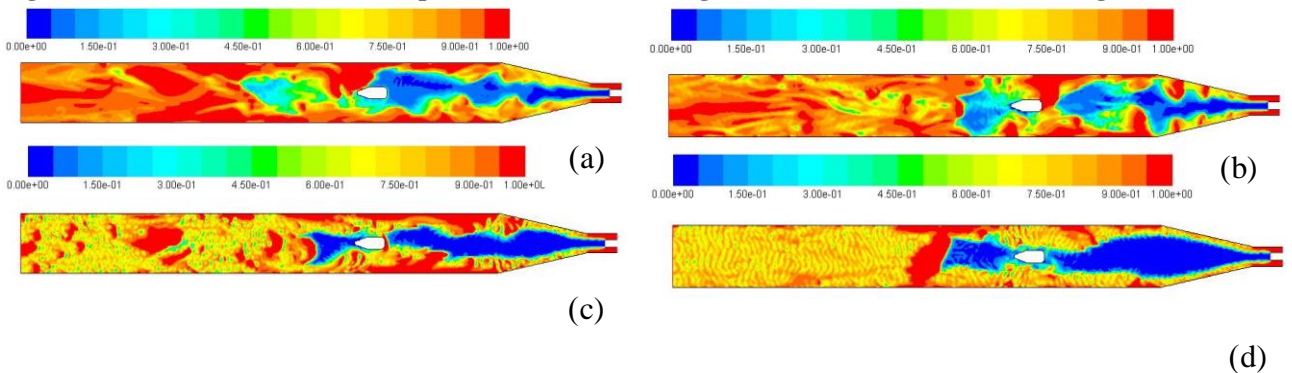


Figure 16. Volume fraction (water) contours for cases (1, 2, 6 and 10) respectively.

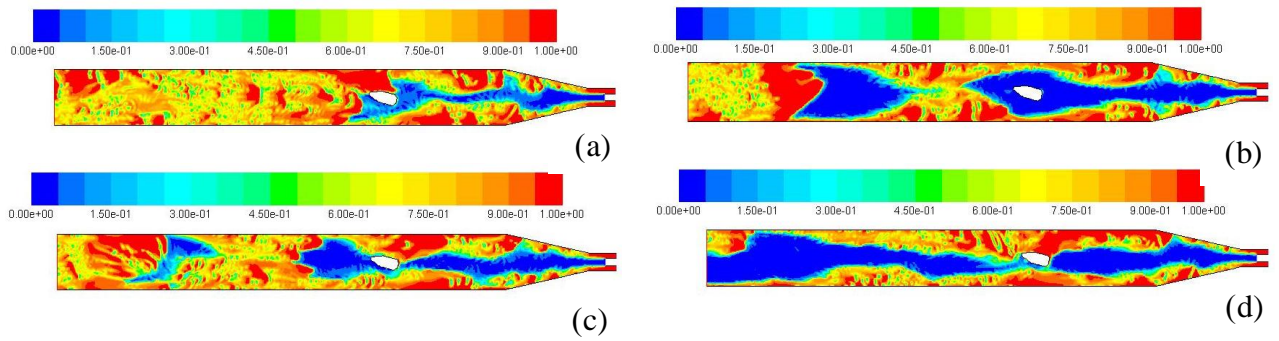


Figure 17. Volume fraction (water) contours for cases (3, 11, 12 and 16) respectively.

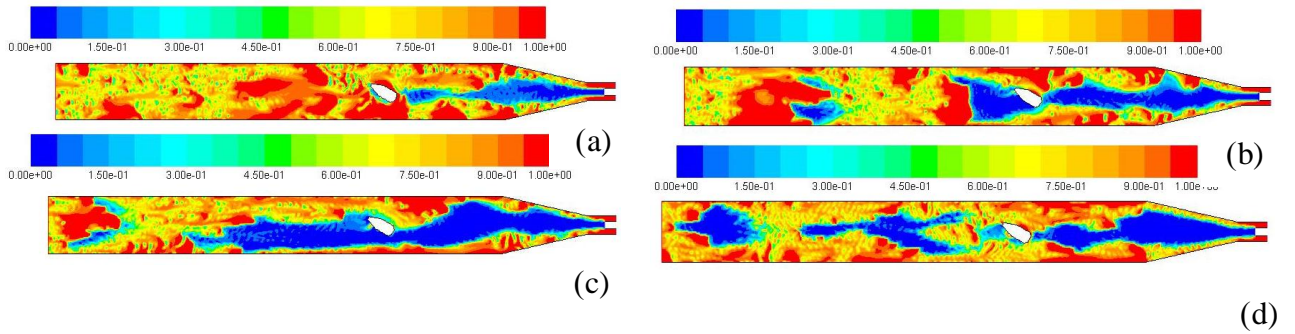


Figure 18. Volume fraction (water) contours for cases (4, 7, 9 and 13) respectively.

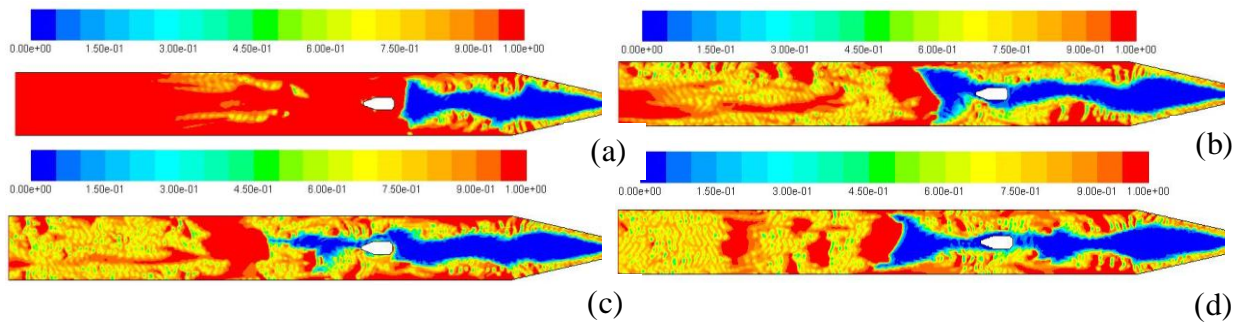


Figure 19. Volume fraction (water) contours development for unsteady case 5.

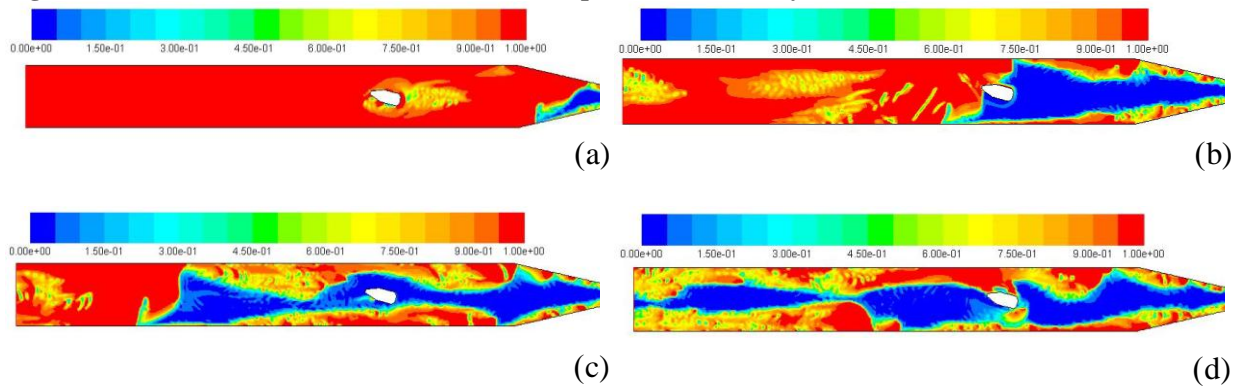


Figure 20. Volume fraction (water) contours development for unsteady case 14.

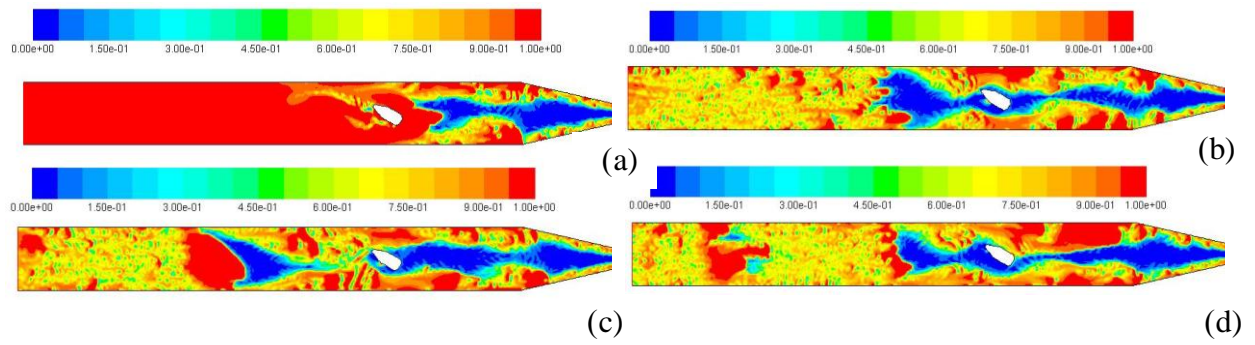


Figure 21. Volume fraction (water) contours development for unsteady case8.

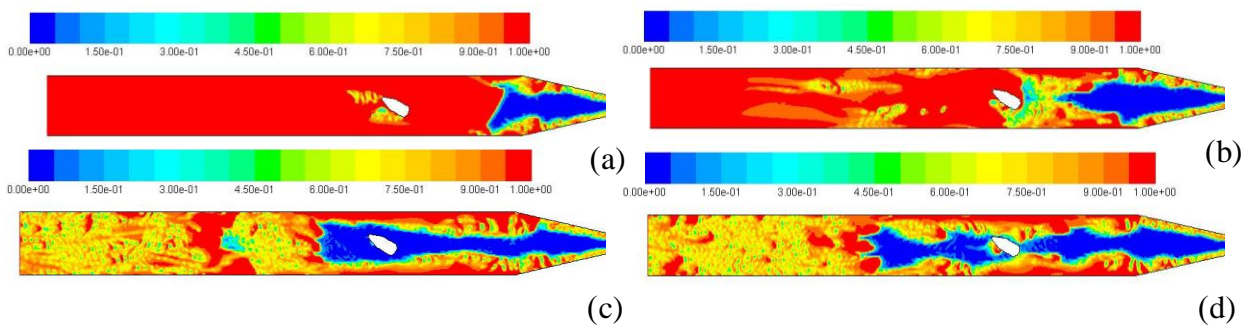


Figure 22. Volume fraction (water) contours development for unsteady case15.